Monthly Notices of the ROYAL ASTRONOMICAL SOCIETY

MNRAS 433, 2097–2106 (2013) doi:10.1093/mnras/stt885
Advance Access publication 2013 June 18

Lucky imaging of transiting planet host stars with LuckyCam

F. Faedi,[1★†] T. Staley,[2] Y. Gómez Maqueo Chew,[3,1] D. Pollacco,[1] S. Dhital,[3,4] S. C. C. Barros,[5] I. Skillen,[6] L. Hebb,[3] C. Mackay[2] and C. A. Watson[7]

[1]Department of Physics, University of Warwick, Coventry CV4 7AL, UK
[2]Institute of Astronomy, Cambridge University, Madingley Road, Cambridge CB3 0HA, UK
[3]Department of Physics and Astronomy, Vanderbilt University, Nashville, TN 37235, USA
[4]Department of Astronomy, Boston University, 725 Commonwealth Avenue, Boston, MA 02215, USA
[5]Aix Marseille Université, CNRS, LAM (Laboratoire d'Astrophysique de Marseille) UMR 7326, 13388 Marseille, France
[6]Isaac Newton Group of Telescope, Apartado de Correos 321, Santa Cruz de la Palma 38700, Spain
[7]Astrophysics Research Centre, Queen's University Belfast, University Road, Belfast BT7 1NN, UK

Accepted 2013 May 15. Received 2013 May 14; in original form 2013 April 29

ABSTRACT

We obtained high-resolution, high-contrast optical imaging in the Sloan Digital Sky Survey i' band with the LuckyCam camera mounted on the 2.56 m Nordic Optical Telescope, to search for faint stellar companions to 16 stars harbouring transiting exoplanets. The Lucky imaging technique uses very short exposures to obtain near diffraction-limited images yielding sub-arcsecond sensitivity, allowing us to search for faint stellar companions within the seeing disc of the primary planet host. Here, we report the detection of two candidate stellar companions to the planet host TrES-1 at separations <6.5 arcsec and we confirm stellar companions to CoRoT-2, CoRoT-3, TrES-2, TrES-4 and HAT-P-7 already known in the literature. We do not confirm the candidate companions to HAT-P-8 found via Lucky imaging by Bergfors et al., however, most probably because HAT-P-8 was observed in poor seeing conditions. Our detection sensitivity limits allow us to place constraints on the spectral types and masses of the putative bound companions to the planet host stars in our sample. If bound, the stellar companions identified in this work would provide stringent observational constraints to models of planet formation and evolution. In addition, these companions could affect the derived physical properties of the exoplanets in these systems.

Key words: instrumentation: high angular resolution – methods: observational – planetary systems.

1 INTRODUCTION

More than 800 extrasolar planets have been discovered to date showing a large variety of physical and dynamical properties that are dramatically different from those observed in our Solar system. This has revolutionized our understanding of planetary formation, structure and evolution. One-third of the known gas giant planets orbit their host at separations smaller than a few tenths of an au (with orbital periods $P < 10$ d). Among these, transiting systems are especially important as they allow accurate measurements of masses, radii, and hence densities, to be derived. These key parameters inform us of the system's physical properties, and can constrain theoretical evolutionary models (e.g. Guillot 2005; Burrows et al. 2007; Fortney, Marley & Barnes 2007; Liu, Burrows & Ibgui 2008). In contrast to the planets in our Solar system, exoplanets show a large variety of orbital properties, for example their orbital eccentricities span a wide range $e = 0$–0.97 (e.g. HD 80606, Eggenberger, Udry & Mayor 2004; Pont, Hébrard & Irwin 2009; HAT-P-13, Bakos et al. 2009). The close-in 'hot Jupiters' show a large angular distribution of (mis)alignments with respect to their host stars' rotation axis (Triaud et al. 2010; Winn et al. 2010, 2011; Morton & Johnson 2011), and some exoplanets even have retrograde orbits (e.g. WASP-17; Anderson et al. 2010).

To explain the observed exoplanet orbital configurations, different scenarios have been proposed for migrating the planets inwards from beyond the snow line to their observed position. These migration mechanisms make different predictions about the current orbital configurations of the planetary systems. For example, planet–disc interaction via angular momentum exchange (e.g. Lin, Bodenheimer & Richardson 1996; Ida & Lin 2004) results in damping any initial inclination of the planetary orbit with respect to the disc (see e.g. Marzari & Nelson 2009; Watson et al. 2011).

★ E-mail: f.faedi@warwick.ac.uk
† Part of this work was carried out while at Queens University Belfast.[7]

Alternatively, gravitational interaction among multiple giant planets (planet–planet scattering; e.g. Wu & Murray 2003; Nagasawa, Ida & Bessho 2008), and perturbations induced by a companion star or a more distant massive planet (Kozai mechanisms; see Fabrycky & Tremaine 2007) result in orbital configurations with large spin–orbit misalignments and large eccentricities (Rasio & Ford 1996; Weidenschilling & Marzari 1996; Chatterjee et al. 2008).

Observational evidence for planet–disc migration is found in multiplanetary systems with mean-motion resonant orbits (e.g. GJ 876, Lee & Peale 2002; Crida, Sándor & Kley 2008). On the other hand, measurements of the Rossiter–Mclaughlin effect[1] (McLaughlin 1924; Rossiter 1924) suggest that ∼40 per cent of transiting planets have highly tilted orbits providing supporting evidence for planet–planet scattering and the Kozai migration mechanism (Winn et al. 2009b; Winn 2010). Examples of systems with large spin–orbit misalignments and/or high eccentricities are, respectively, WASP-17b (Anderson et al. 2010), HAT-P-7b (e.g. Winn et al. 2009a) and HD80806b (e.g. Eggenberger et al. 2004; Pont et al. 2009; Hébrard et al. 2010). More recently, Albrecht et al. (2012) suggested that the Kozai mechanism is responsible for the migration of the majority, if not all, hot Jupiters, both misaligned and aligned, and that star–planet tidal interaction plays a central role in shaping exoplanets orbital configurations.

In this paper, we present high-contrast, high angular resolution optical imaging for 16 stars harbouring transiting extrasolar planets to search for faint stellar companions. Identifying binary companions to known planet hosts can provide observational evidence to constrain the different formation and evolution scenarios, as well as provide crucial information for subsequent exoplanet characterization (see also Daemgen et al. 2009; Narita et al. 2012; Bergfors et al. 2013). The presence of a close-in stellar source to a transiting planet host star, as in the case for WASP-12 (Bergfors et al. 2013, via Lucky imaging), could affect the derived planetary parameters by diluting the transit signal (see also Daemgen et al. 2009). For example, Crossfield et al. (2012) find that WASP-12b is rather hotter and slightly larger (by 1–2 per cent) than previously reported, highlighting the importance of high-resolution imaging for the characterization of known and newly discovered transiting planetary systems. Additionally, the presence of an M dwarf only 1 arcsec from WASP-12 might have contaminated past atmospheric measurements, possibly challenging the detection of a high atmospheric C/O ratio for WASP-12b (see Madhusudhan et al. 2011; Crossfield et al. 2012 for a recent re-analysis).

The paper is organized as follows: in Section 2, we briefly describe our Lucky imaging technique; Section 3 presents our LuckyCam observations; in Section 4, we explain the data reduction, image analysis and candidate detection. Our results are presented in Section 5, including the non-detections in our sample. In Section 6, we discuss the likelihood of the detected companions being bound to the planet hosts. Finally, we summarize our findings and conclusions in Section 7.

2 LUCKY IMAGING TECHNIQUE

Lucky imaging consists of the acquisition of short exposures, at a rate of a few tens of frames per second, using a very low noise electron multiplying CCD camera (Fried 1978; Baldwin et al. 2001; Tubbs et al. 2002; Mackay et al. 2004; Law, Mackay & Baldwin 2006). This allows the rapid image motion due to atmospheric turbulence to be corrected. Because the perturbations introduced by the atmosphere change on time-scales of a few milliseconds (known as the atmospheric coherence time), with fast imaging each frame captures a different point spread function (PSF) resulting from the atmospheric turbulence at that particular moment. By monitoring the rapid PSF variations, we can select high-quality short exposures from moments of excellent seeing. During data reduction the best frames are selected, aligned and co-added to produce a final image with a bright diffraction limited core surrounded by a fainter seeing halo. Law et al. (2006) give a detailed explanation on the Lucky imaging technique and the LuckyCam specifications.

3 OBSERVATIONS

Observations were obtained between 2009 July 18 and 22 at the 2.56 m Nordic Optical Telescope (NOT) at the Roque de los Muchachos Observatory, La Palma, with the Cambridge LuckyCam visitor instrument. Seeing ranged from ∼0.6 to ∼1.65 arcsec as measured by the Differential Image Motion Monitor (at 500 nm; Tokovinin 2002). All observations were made in the Sloan Digital Sky Survey (SDSS) i' band, using a plate scale of 32.4 mas pixel^{-1}, providing good sampling of the PSF. The camera frame rate was 20.75 frames per second using full chip readout (1024 pixels squared). Table 1 presents a summary of our observations. Targets were often observed slightly off-centre on the CCD detector to achieve better positioning of the mosaic field of view for astrometric calibration. The target observed closest to the CCD edge has an unbroken observation area of radius 6.5 arcsec. Therefore, to give a uniform data set, we only list detections within 6.5 arcsec. However, we note that the planet host HAT-P-1 (Bakos et al. 2007) is known to be part of a binary system with a companion at ∼11 arcsec, that was clearly detected in our images at a separation $r = 11.26 \pm 0.03$ arcsec, although this target is not discussed further in this paper.

We selected our sample to optimize the number of planet host stars observable as by 2009 July, in order to cover a large parameter space of different stellar and planetary properties. Detailed information on individual objects is available from the Exoplanet Encyclopaedia.[2] We present our sample in Table 1, separating the planet host stars with candidate companions detected in this work from those without detections.

4 DATA REDUCTION, IMAGE ANALYSIS AND CANDIDATE DETECTION

4.1 Data reduction

The data were reduced using the LuckyCam pipeline. Standard bias correction, gain calibration and cosmic ray removal was applied. The LuckyCam pipeline registers the image motion of each exposure using an interpolated cross-correlation algorithm (Law et al. 2006; Staley & Mackay 2010). The peak of the cross-correlation map provides a proxy for the Strehl ratio (i.e. the peak value of the PSF divided by the theoretical diffraction-limited value, commonly used as a high-resolution imaging performance metric) and estimates the relative exposure quality (Staley & Mackay 2010). For each data set, re-centred and drizzled (Fruchter & Hook 2002) images are produced by the pipeline which then selects and co-adds observed frames that meet the image quality criteria as described

[1] See the Holt–Rossiter–McLaughlin Encyclopaedia; http://www.aip.de/People/rheller/content/main_spinorbit.html.

[2] http://exoplanet.eu/

Table 1. The sample of 16 stars harbouring transiting extrasolar planets studied in this paper. We list the spectral type and the orbital eccentricity (e) [2], λ the measured spin–orbit (mis)alignment angle (data and references taken from the Rossiter–Mclaughlin encyclopaedia[1]), the number of observed frames and the total exposure times for the 100 per cent selection images of LuckyCam, and the average seeing at 500 nm.

Target	SpT	e	λ (deg)	N_{frames}	T_{exp} (s)	Seeing (arcsec)
HAT-P-1	G0V	0.067	3.7 ± 2.1	5400	260	0.65
HAT-P-2	F8V	0.52	$1.2 \pm 13.4/0.2^{+12.2}_{-12.5}/9 \pm 10$	8000	384	0.99
HAT-P-5	G1V	0	–	9000	432	1.02
HAT-P-6	F8V	0	$166 \pm 10/165 \pm 6$	5000	240	0.66
HAT-P-8[a]	F	0	$-9.7^{+9.0}_{-7.7}/-17^{+9.2}_{-11.5}$	9100	437	1.51
HAT-P-11	K4V	0.19	$103^{+22}_{-18}/103^{+26}_{-10}/106^{+15}_{-11}/97^{+8}_{-4}$	6000	288	0.64
HD 209458	G0V	0	$3.9^{+18}_{-21}/-4.4 \pm 1.4/-5 \pm 7$	10 000	480	0.96
WASP-3	F7V	0	$13^{+9}_{-7}/3.3^{+2.5}_{-4.4}/5^{+6}_{-5}$	10 000	480	1.11
WASP-3	”	”	”	5000	240	0.65
WASP-10	K5V	0.05	–	5000	240	0.74
XO-1	G1V	0	–	10 000	480	0.79
Targets with candidate companions from this work						
CoRoT-2[b]	G7V	0	$7.2 \pm 4.5/-1^{+6}_{-7.7}/4.7 \pm 12.3$	6000	288	1.37
CoRoT-3[c]	F3V	0	$-37.6^{+22.3}_{-10}$	5174	248	1.44
HAT-P-7[d]	F6V	0	$182.5 \pm 9.4/-132.6^{+10.5}_{-16.3}/155 \pm 37$	5175	248	1.10
TrES-1	K0V	0	30 ± 21	7700	370	0.88
TrES-2[e]	G0V	0	-9 ± 12	7000	336	0.83
TrES-4[e]	F8V	0	6.3 ± 4.7	10 000	480	1.12

[a]Candidate companion identified by Bergfors et al. (2013).
[b]Candidate companion identified by Alonso et al. (2008).
[c]Candidate companion identified by Deleuil et al. (2008).
[d]Candidate companion identified by Narita et al. (2010).
[e]Candidate companion identified by Daemgen et al. (2009).

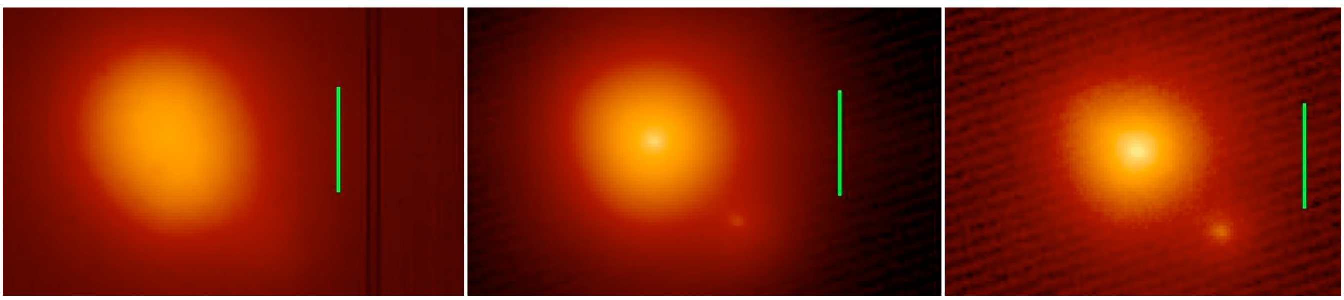

Figure 1. Images of TrES-2 obtained with LuckyCam showing the image quality improvement due to the Lucky imaging technique. Left-hand panel shows a simple average corresponding to a conventional long exposure. The middle and right-hand panels show images resulting from re-centring and drizzling the short exposures with 100 and 5 per cent selection cutoffs, respectively. All images have the same log scale. The green bar depicts 1 arcsec line. Average seeing during these observations was 0.8 arcsec.

in detail by Law et al. (2006) and Staley & Mackay (2010). This procedure yields two images for each data set, the first obtained by co-adding the sharpest 5 per cent selection of the frames, and the second by co-adding all exposures (100 per cent; see for example Fig. 1 – *middle panel*). When choosing the selection cutoff there is a trade-off to be made between a smaller full width at half-maximum (FWHM) at low-percentage cutoffs (from fewer images with higher Strehl ratio), and lower pixel noise at high-percentage cutoffs, due to longer cumulative exposure time. Fig. 1 shows the improvement obtained with Lucky imaging for the case of the planet hosting star, TrES-2 (see also Law et al. 2006, fig. 2).

The NOT telescope is subject to aberrations and does not yield near diffraction-limited images (see e.g. http://www.not.iac.es/telescope/tti/imqual.pdf). A combination of small-scale mirror irregularities and chromatic dispersion effects limit the probability of obtaining diffraction-limited images although the large number of images and the random phase variation of the atmosphere can compensate for slight aberrations and telescope focusing.

Additionally, our Lucky imaging data do not show ‘quasi-static speckles’, as in adaptive optics (AO) imaging (see e.g. Boccaletti et al. 2003, 2004; Marois et al. 2003; Hinkley et al. 2007), that could be mistaken for faint companions. Our data were visually inspected in order to confirm the presence of faint companion candidates throughout the data reduction process. Furthermore, other possible causes of false detection such as ‘ghosting’ were not observed in our data.

4.2 Image analysis

The technique most widely applied when attempting to identify faint or crowded point sources in astronomical images is that of PSF fitting and subtraction. A step crucial to this process is the choice and evaluation of PSF models, which may be derived semi-analytically (Dolphin 2000), empirically (Diolaiti et al. 2000) or by some combined analytical model fitted with empirical corrections (Stetson 1987). In the case of Lucky imaging, we expect the PSF to be symmetric; however, it is not trivial to model the radial profile as the PSF consists of a narrow core surrounded by a wide halo (e.g. Hardy 1998). Our image analysis algorithm is described below in three steps:

(1) *PSF subtraction*. To create an axisymmetric, semi-empirical model of the PSF, we perform a Gaussian fit of 9 pixels around the brightest, central pixel giving a PSF central position to sub-pixel precision. The flux values in the pixels around the nominal centre are collected into bins (in radius) and a median and standard deviation are evaluated at approximately one pixel-width radius intervals. Any visually identified candidate in our images is masked off during this process so as not to contaminate the PSF model. The Gaussian fit is used within 1.5 pixels radius from the PSF centre, while at larger radii the model is generated using interpolated median values from the annulus bins. Finally, the PSF model is subtracted from the original image to give a residual image shown in Fig. 2 (bottom left).

(2) *Background subtraction via median boxcar filter*. After the axisymmetric PSF model has been subtracted, some artefacts can remain in the image that might hamper attempts to identify companion stars. In order to validate our detections, we employed a median boxcar filter to suppress any artefacts present. For every pixel, the background level is estimated by taking the median of all pixel values within a circular aperture of radius 7 pixels (i.e. small enough to suppress localized background variations, whilst remaining significantly larger than the PSF core so that companion candidates are not removed). The 'background map' of median values is then subtracted from the residual image (see top right, Fig. 2).

(3) *Convolution with a Gaussian Profile*. For this relatively small data set, we visually inspected all the sources, utilizing a Gaussian convolution of the resulting images from Step 2 to enhance visibility of any companion candidate (see bottom right, Fig. 2). Once a candidate has been re-identified, the location is inspected in images from all stages of the image analysis process (i.e. reduced image, PSF-subtracted image and background subtracted image) in order to verify that the candidate is not a detector artefact or arising from the image analysis process.

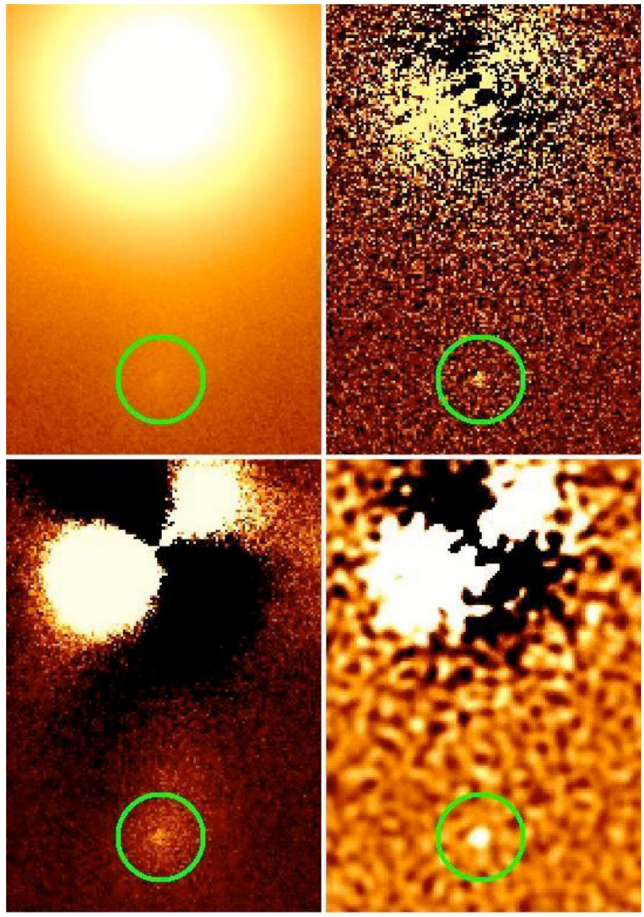

Figure 2. Different stages of the analysis of HAT-P-7. Top left: the image output from the LuckyCam pipeline with the 5 per cent selection criterion. Bottom left: after PSF subtraction, Step 1 of the image analysis algorithm (described in Section 4.2). Top right: after background subtraction via a median boxcar filter (Step 2). Bottom right: after Gaussian convolution (Step 3). The identified close companion to HAT-P-7 is circled (north is left and east is down).

4.3 Candidate detection

Our detection threshold was chosen to be four times the standard deviation of the background (σ) at any given concentric circle at increasing separations from the centre of the planet host. The sensitivity of our observations to detect stellar companions at different angular separations from the primary planet host is given in Table 2. We place upper limits in $\Delta i'$ to the presence of stellar companions to all targets at angular separations of 0.25, 0.5, 1, 2.5 and 6.5 arcsec from the centre of the primary. The adopted 4σ detection limits depend on the exposure time and primary target magnitude as well as seeing. This is exemplified in Fig. 3 where we plot our detection sensitivity as a function of angular separation in the case of WASP-3 during observations obtained over two consecutive nights with different seeing conditions. The first set of 10 000 images were obtained with an average seeing of 1.11 arcsec while the second 5000 images were obtained with an average seeing of 0.65 arcsec. The effect of poorer image quality is particularly evident at small separations within the seeing disc of the planet host star. Even though, the first set of data have twice the number of frames, the images taken during better seeing conditions allow the detection of companions $\Delta i' = 1.8$ mag fainter at a separation of 0.25 arcsec. Fig. 4 shows our average sensitivity. We depict our results in black circles and our non-detections in red circles. These are discussed in detail in Appendix A. Additionally, we report the minimum, average and maximum sensitivity curves (grey dashed, dot–dashed lines) derived for the sample of host stars with no visually detected companions. Typically, we can detect companions that are $\Delta i' \sim 4$ magnitudes fainter than the primary at a distance of 0.25 arcsec. As expected, our sensitivity to fainter companions increases with increasing distance from the planet host.

Once a candidate companion has been identified, it is verified as a bona fide stellar source by excluding it as a product of the data and/or image analysis as follows. First, the FWHM of the planet host is measured from our images. Secondly, the flux of the primary star is measured using a circular aperture of diameter 6×FWHM on these images. Thirdly, on the PSF-subtracted images, a Gaussian

Table 2. The 4σ detection limits (in $\Delta i'$) for all stars in our sample with and without detected companions at separations of $r = 0.25$, 0.5, 1, 2.5 and 6.5 arcsec.

		4σ detection limits ($\Delta i'$)				
Target	r(arcsec)	0.25	0.5	1.0	2.5	6.5
HAT-P-1		3.57	4.12	7.62	8.99	9.22
HAT-P-2		4.17	4.51	6.21	8.16	8.23
HAT-P-5		3.81	4.05	6.04	7.50	7.70
HAT-P-6		3.63	4.78	7.50	8.87	9.12
HAT-P-8		4.67	4.73	5.75	7.52	7.97
HAT-P-11		3.29	4.54	7.58	9.51	9.72
HD 209458		4.32	4.42	7.12	9.24	9.31
WASP-10		3.86	4.38	6.39	7.31	7.41
WASP-3[b]		4.36	4.03	7.08	8.78	9.18
WASP-3[a]		2.66	4.31	5.73	7.71	8.16
XO-1		3.39	4.03	6.80	8.05	8.19
Targets with candidate companions						
CoRoT-2		4.43	4.71	5.36	6.26	6.37
CoRoT-3		4.90	5.09	5.51	5.92	5.89
HAT-P-7		4.14	4.51	5.55	7.43	7.91
TrES-1		4.11	4.52	7.03	7.97	8.02
TrES-2		4.40	5.14	6.82	7.50	7.50
TrES-4		4.19	4.26	6.15	7.86	7.99

[a]Derived from 10 000, compared to [b]5000.

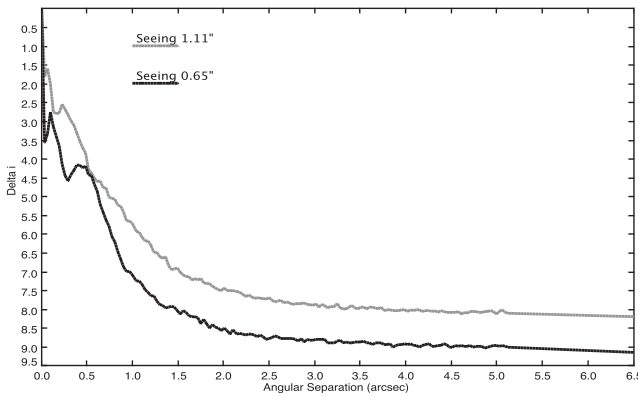

Figure 3. The effect of seeing conditions on our detection sensitivity for the planet host star WASP-3. The first 10 000 exposures were obtained with an average seeing of 1.11 arcsec and the second 5000 frames with an average seeing of 0.65 arcsec. The data set obtained during better seeing conditions shows an increase in detection sensitivity, important at small separations within the seeing disc of the primary star.

fit is used to determine the central pixel position of the candidate companion. Then, the flux of the identified companion is measured on the PSF subtracted image, similarly to the primary flux measurement. Finally, the signal-to-noise ratio (SNR) of the companion (see Table 3) is calculated taking into account background and photon shot noise using the following equation:

$$\mathrm{SNR} = \frac{F - N_{\mathrm{pix}} b}{\sqrt{N_{\mathrm{pix}} \sigma_a^2 + F}}, \quad (1)$$

where b and σ_a^2 are the mean value and variance of the background pixels within the aperture of the companion, F is the flux over the number of pixels in the photometric aperture, N_{pix}. The SNR values for the candidate companions identified in this work are given in Table 3.

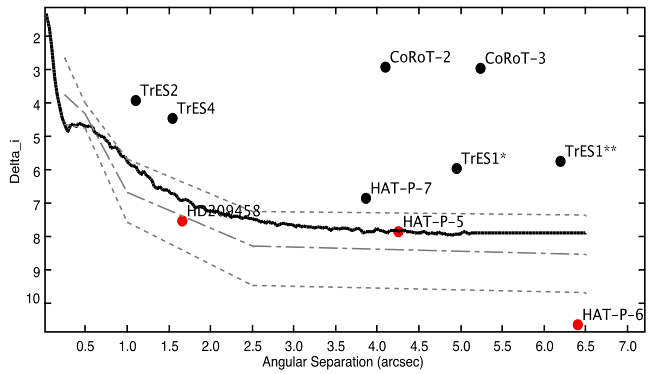

Figure 4. Average sensitivity of the LuckyCam survey (black line). We indicate our detections with black circles and the three non-detections discussed in Appendix A with red circles. The grey dashed and the dot–dashed lines indicate our minimum, maximum and average detection limits (see Table 2) for the sample of host stars with no visual companion detected.

Table 3. Results for the planet hosting stars with detected candidate stellar companions from this work. From left to right, we list the name of the planet host, the angular separation of the candidate companion, the position angle, the $\Delta i'$ magnitude and the SNR of the detected companion.

Target	r (arcsec)	PA (°)	$\Delta i'$ (mag)	SNR
CoRoT-2	4.10 ± 0.03	208.4 ± 0.4	2.95 ± 0.03	41
CoRoT-3	5.24 ± 0.03	173.9 ± 0.4	3.0 ± 0.1	10
HAT-P-7	3.87 ± 0.03	90.4 ± 0.5	6.9 ± 0.1	10
TrES-1	4.95 ± 0.03	149.6 ± 0.5	6.02 ± 0.08	14
TrES-1	6.19 ± 0.03	47.4 ± 0.2	5.79 ± 0.07	17
TrES-2	1.11 ± 0.03	137 ± 2	3.97 ± 0.01	86
TrES-4	1.54 ± 0.03	1.2 ± 1.2	4.51 ± 0.02	52

5 RESULTS

In the sample of 16 transiting planet host stars, we have detected candidate companion stars for six planet hosts TrES-1, TrES-2, TrES-4, HAT-P-7, CoRoT-2 and CoRoT-3. Each candidate companion has been identified from visual inspection of the reduced Lucky imaging frames as described in Section 4.3. We summarize our results in Table 3 where we give the relative photometry and astrometry of the companion candidates. To have a uniform data set, we only list detections within 6.5 arcsec from the centre of the planet host star.

Our LuckyCam images clearly show the presence of two candidate companions to the planet hosts star TrES-1, previously unknown. Fig. 5 shows the LuckyCam images for TrES-1 and the candidate companions identified in this work.

Among our sample TrES-2, TrES-4 and HAT-P-7 have previously published high-resolution AO and/or Lucky imaging observations showing the presence of faint stellar companions (Daemgen et al. 2009; Narita et al. 2010; Bergfors et al. 2013). Additionally, the companion stars to CoRoT-3 (2MASS J19281330+0007135) and CoRoT-2 (2MASS J19270636+0122577), have been identified in previous works see e.g. Deleuil et al. (2008) and Alonso et al. (2008), Gillon et al. (2010), respectively. We note that Deleuil et al. (2008) also mentions a second fainter companion to CoRoT-3 at separation 5.6 arcsec. We do not report this object in our discussion as it falls near the CCD edge making our image analysis unreliable. The companion to CoRoT-2 and the two companions to HAT-P-7 have also been confirmed to be bound to the planet-hosting stars,

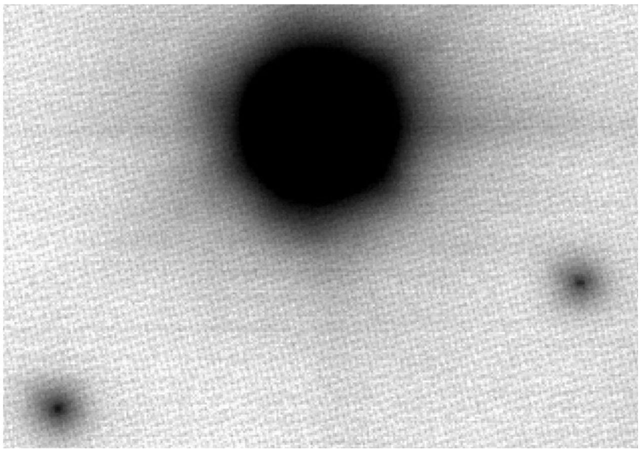

Figure 5. The LuckyCam images for the planet host star TrES-1. North is left and east is down. The two companions are clearly visible in our images.

forming wide binary systems (Schröter et al. 2011; Narita et al. 2012). We confirm previous findings for the companions to TrES-2 and TrES-4, while for HAT-P-7 we can only detect the brighter of the two companions found by Narita et al. (2010, 2012). The authors estimated the fainter companion to HAT-P-7 to be of spectral type M9−L0 ($m_2 \simeq 0.078$–$0.088\ M_{\odot}$) at a separation of 3.14 ± 0.01 arcsec, and therefore is below our detection limit for these observations, see Tables 2 and 4. Our results for the position angles, spectral type determinations and separations for the companions to CoRoT-2, TrES-2, TrES-4 and HAT-P-7 agree with the results obtained by Alonso et al. (2008), Gillon et al. (2010), Schröter et al. (2011), Daemgen et al. (2009), Narita et al. (2010, 2012) and Bergfors et al. (2013), and are presented in Tables 5 and 6. In the case of the planet host star HAT-P-8, we are unable to confirm the candidate companion identified by Bergfors et al. (2013). The sensitivity of our observations of HAT-P-8 at the separation of 1.027 arcsec would only allow us to detect companions two magnitudes brighter than the detection reported by the authors.

5.1 Non-detections

Our visual inspection of the LuckyCam images showed no stellar companions to the following planet host stars: HAT-P-1, HAT-P-2, HAT-P-5, HAT-P-6, HAT-P-8, HAT-P-11, HD 209458, WASP-10, WASP-3 and XO-1. Our results are in agreement with previous studies with the exception of HAT-P-8 for which our reduced image quality does not allow the identification of the companion reported by Bergfors et al. (2013). Finally, in the cases of HD 209458, HAT-P-5 and HAT-P-6 our visual inspection of the images shows possible candidate companions to the planet hosts, however, after further consideration (discussed in appendix A), these putative identifications are classified as non-detections.

6 STATISTICAL LIKELIHOOD OF ASSOCIATION

The detection of faint stellar companions associated with our targets could provide important observational constraints for theoretical models of planet formation and evolution. We used a statistical approach to investigate the probability of each detected companion star being gravitationally bound to the planet host. We first estimated the density of background sources $\rho(m)$ in a cone of 10 arcmin around each target. Because our targets are quite bright we used the Two Micron All Sky Survey (2MASS; Skrutskie et al. 2006) catalogue to retrieve objects within the 10 arcmin cone around the planet host coordinates. Subsequently, we derive the probability that a target star has a non-related background source within the separation of the detected candidate companions. By using a similar method to that adopted by Daemgen et al. (2009), we used the 2MASS magnitudes to identify bright giant stars in the ensemble of retrieved objects. We selected all objects with $J - Ks > 0.5$ and with $K < 15$, which corresponds to the background detection

Table 4. Upper limits for companions' spectral types and masses for the 16 planet host stars in our sample at separations $r = 0.25$, 0.5, 1, 2.5 and 6.5 arcsec from the primary.

Target	$r = 0.25$ arcsec		$r = 0.5$ arcsec		$r = 1$ arcsec		$r = 2.5$ arcsec		$r = 6.5$ arcsec	
	Sp.T ±1	m_2 ($M_{\odot}$)	Sp.T ±1	m_2 ($M_{\odot}$)	Sp.T ±1	m_2 ($M_{\odot}$)	Sp.T ±1	m_2 ($M_{\odot}$)	Sp.T ±1	m_2 ($M_{\odot}$)
HAT-P-1	K7–M0	0.63–0.59	M1–M2	0.54–0.42	M5	0.15	M7	0.11	M7	0.11
HAT-P-2	M0–M1	0.59–0.54	M1–M2	0.54–0.42	M4–M5	0.20–0.15	M7	0.11	M7	0.11
HAT-P-5	M0	0.59	M1	0.54	M4–M5	0.20–0.15	M6	0.12	M6	0.12
HAT-P-6	M0	0.59	M2	0.42	M5	0.15	M6	0.12	M7	0.11
HAT-P-8	M2	0.42	M2	0.42	M4	0.20	M6	0.12	M6	0.12
HAT-P-11	M2	0.42	M5	0.15	M6–M7	0.12–0.11	L0	0.078	>L0	<0.078
HD 209458	M1–M2	0.54–0.42	M2	0.42	M5	0.15	M6–M7	0.12–0.11	M7	0.11
WASP-3[a]	K5	0.70	M1	0.54	M4–M5	0.20–0.15	M6	0.12	M6	0.12
WASP-3[b]	M0	0.59	M0–M1	0.59–0.54	M4	0.20	M7	0.11	M7	0.11
WASP-10	M4	0.20	M4–M5	0.20–0.15	M6–M7	0.12–0.11	M8	0.102	M8	0.102
XO-1	K7	0.63	M1–M2	0.54–0.42	M5	0.15	M6–M7	0.12–0.11	M6–M7	0.12–0.11
Targets with companion candidates										
CoRoT-2	M2–M3	0.42–0.29	M3	0.29	M4	0.20	M4–M5	0.20–0.15	M5	0.15
CoRoT-3	M2	0.42	M1	0.54	M2	0.42	M3	0.29	M3	0.29
HAT-P-7	M1	0.54	M1	0.54	M3–M4	0.29–0.20	M5–M6	0.15–0.12	M6	0.12
TrES-1	M2–M3	0.42–0.29	M3–M4	0.29–0.20	M6	0.12	M7–M8	0.11–0.102	M7	0.11
TrES-2	M1–M2	0.54–0.42	M3	0.29	M5	0.15	M6–M7	0.12–0.11	M6–M7	0.12–0.11
TrES-4	M0	0.59	M1	0.54	M4–M5	0.20–0.15	M6	0.12	M6–M7	0.12–0.11

Table 5. Companion candidates for six planet host stars. From left to right, we list the name of the planet host star, separation angle, the position angle, the $\Delta i'$ for the detected companions, the SNR of the detected companion, the probability for the companion to be a chance alignment ($\mathcal{P}(\Theta, m)$) and the expected number of sources with an unrelated background companion (E_{bg}), the probability of a chance alignment detection as estimated by Dhital et al. (2010), the planet host's distance (pc) and finally the companion separation in au, assuming the value is a lower limit.

Target	r (arcsec)	PA (°)	$\Delta i'$ (mag)	SNR	$\mathcal{P}(\Theta, m)$ (per cent)	E_{bg}	$\mathcal{P}_{D10}$ (per cent)	Dist. (pc)	Sep. (au)
CoRoT-2	4.10 ± 0.03	208.4 ± 0.4	2.95 ± 0.03	41	3.17	0.22	1.18	270 ± 120	1108 ± 492
CoRoT-3	5.24 ± 0.03	173.9 ± 0.4	3.0 ± 0.1	10	4.05	0.12	1.72	680 ± 160	3562 ± 838
HAT-P-7	3.87 ± 0.03	90.4 ± 0.5	6.9 ± 0.1	10	0.03	0.004	0.2	320 ± 50	1238 ± 193
TrES-1	4.95 ± 0.03	149.6 ± 0.5	6.02 ± 0.08	14	0.82	0.025	0.04	150 ± 6	743 ± 30
TrES-1	6.19 ± 0.03	47.4 ± 0.2	5.79 ± 0.07	17	1.29	0.039	0.06	150 ± 6	929 ± 37
TrES-2	1.11 ± 0.03	137 ± 2	3.97 ± 0.01	86	0.03	0.0005	0	220 ± 10	244 ± 13
TrES-4	1.54 ± 0.03	1.2 ± 1.2	4.51 ± 0.02	52	0.03	0.0007	0	479 ± 26	740 ± 43

Table 6. Estimated absolute i' magnitudes (M_i'), spectral types and masses for the companion stars, derived assuming binarity for each companion. Values for the companions are derived from Kraus & Hillenbrand (2007) and Baraffe et al. (1998) models using published 2MASS magnitudes, distances and T_{eff} of the planet host targets. Magnitude errors are estimated through propagation of the known errors on the target *J, H, K* magnitude and distances. Superscript ^{1} and ^{2} indicate the host star and the companion(s), respectively.

Target	J^1	H^1	K^1	M_J^1	M_H^1	M_K^1	SpT^1	T_{eff}^1 (K)	$M_{i'}^1$	$\Delta i'$ (mag)	$M_{i'}^2$	SpT^2	m_2 ($M_\odot$)
CoRoT-2[a]	10.78 ± 0.02	10.44 ± 0.02	10.31 ± 0.019	3.63 ± 0.20	3.28 ± 0.22	3.15 ± 0.22	G7	5608 ± 37	4.60	2.95	7.55	M0	0.59
CoRoT-3	11.94 ± 0.02	11.71 ± 0.02	11.62 ± 0.019	2.77 ± 0.22	2.55 ± 0.22	2.46 ± 0.22	F3	6740 ± 140	3.50	3.00	6.45	K4–K5	0.75–0.70
HAT-P-7[a]	9.55 ± 0.02	9.34 ± 0.02	9.33 ± 0.020	2.03 ± 0.29	1.82 ± 0.29	1.81 ± 0.29	F6	6350 ± 80	4.00	6.92	10.92	M4–M5	0.20–0.15
TrES-1	10.29 ± 0.03	9.89 ± 0.04	9.82 ± 0.030	4.41 ± 2.25	4.01 ± 2.26	3.94 ± 2.25	K0	5214 ± 23	5.47	6.02	11.49	M5	0.15
TrES-1	10.29 ± 0.03	9.89 ± 0.04	9.82 ± 0.030	4.41 ± 1.21	4.01 ± 1.22	3.94 ± 1.21	K0	5214 ± 23	5.47	5.80	11.27	M5	0.20–0.15
TrES-2	10.23 ± 0.03	9.93 ± 0.03	9.85 ± 0.020	3.52 ± 0.81	3.21 ± 0.81	3.13 ± 0.80	G0	5850 ± 50	4.44	3.97	8.41	M1–M2	0.54–0.42
TrES-4	10.58 ± 0.02	10.35 ± 0.02	10.33 ± 0.020	2.18 ± 0.40	1.95 ± 0.40	1.93 ± 0.40	F8	6200 ± 75	4.26	4.50	8.76	M2	0.42
Non-detections													
HD 209458	6.59 ± 0.02	6.37 ± 0.02	6.31 ± 0.020	3.23 ± 0.46	3.00 ± 0.46	2.94 ± 0.46	G0	6075 ± 33	4.40	7.57	11.97	M5–M6	0.15–0.12
HAT-P-5	10.84 ± 0.02	10.52 ± 0.03	10.48 ± 0.020	3.17 ± 0.25	2.85 ± 0.26	2.81 ± 0.25	G1	5960 ± 100	4.40	7.91	12.31	M6	0.12
HAT-P-6	9.56 ± 0.02	9.44 ± 0.04	9.31 ± 0.030	2.47 ± 0.25	2.36 ± 0.27	2.23 ± 0.26	F8	6570 ± 80	3.69	10.69	14.38	M7–M8	0.10

[a]Confirmed bound companions.

limit in these short accumulated exposures (see T_{exp} in Table 1).[3] There is a degeneracy in the near-IR colours of giant and dwarf stars for early spectral types (earlier than K7 or $J - Ks > 0.5$), but these become distinct in two-colour diagrams for the latest spectral types (Majewski et al. 2003). Jurić et al. (2008) used a model of our Galaxy to estimate the number of giant stars which could be misidentified as main-sequence stars and found that the overall bias in the estimated number density is ∼4 per cent within 500 pc. Finally, we used equation (1) from Brandner et al. (2000) to find the probability $\mathcal{P}(\Theta, m)$ for an unrelated source to be located within a certain angular distance Θ from the target.

$$\mathcal{P}(\Theta, m) = 1 - \mathrm{e}^{-\pi \rho(m) \Theta^2}, \quad (2)$$

where Θ is in arcseconds and $\rho(m)$ is the estimated density of background sources within 10 arcmin of the target. We calculated $\mathcal{P}(\Theta, m)$ for each star with a detected faint companion candidate. We also used our images to estimate the expected number of sources in our images with background, not associated, companions (see column 6 of Table 5). We note that all but the *CoRoT* targets have a very low probability of contamination by background sources (see Table 5). The *CoRoT* satellite observes alternatively towards the galactic centre and anticentre, thus increasing the probability of contamination by background objects.

To further test the probability of chance alignment for the binary pairs, we used an independent statistical analysis following the method described in Dhital et al. (2010). We calculated the frequency of unrelated pairings using a Galactic model that is parametrized by an empirically measured stellar number density distribution in a $30 \times 30\,\mathrm{arcmin}^2$ conical volume centred on the candidate binary. The simulated stellar distributions are constrained by empirical measurements from the SDSS (Jurić et al. 2008; Bochanski et al. 2010) and accurately accounts for the decrease in stellar number density with both galactocentric radius and galactic height. All the simulated stars are, by definition, single and unrelated. Therefore, the total the number of simulated stars that are nearby to the candidate primary is the likelihood that the candidate binary is a chance alignment. We performed 10^6 realizations for each of our six candidate binaries. Table 5, columns 6 and 8, show both estimated probabilities $\mathcal{P}(\Theta, m)$ and $\mathcal{P}_{D10}$, respectively. Our results strongly suggest that all the detected faint companions within 6.5 arcsec to our targets are not random chance alignments.

6.1 Companion properties

Under the assumption that the detected companions are bound to the planet host stars in our sample, we used 2MASS magnitudes, spectral types and temperatures (T_{eff}) of the planet host targets to derive spectral types and masses for each candidate companion discussed in Section 5. We first estimated absolute M_J, M_H, M_K magnitudes for each planet host star using their published distances and 2MASS magnitudes. We then used the models given in table 5 of Kraus & Hillenbrand (2007), and models from Baraffe et al. (1998) to evaluate the absolute i' magnitude for the planet hosts interpolating within M_J, M_H, M_K and T_{eff}. In Table 5, we give the estimated $M_{i'}$, spectral types and masses for each candidate

[3] We note however, that for bright guide stars longer observations would have allowed the detection of background sources as faint as $i' \sim 22$ (see e.g. Law et al. 2006).

companion. We note that the candidate companions identified in this study have spectral types later than K4 (see also Daemgen et al. 2009; Narita et al. 2010; Schröter et al. 2011; Bergfors et al. 2013), making them difficult to identify in optical spectra, as well as in optical, seeing-limited photometry.

The faint stellar companions identified to TrES-1 have separations from it larger than 2 arcsec, sufficient to avoid blending effects during spectroscopic and photometric observations. Such effects in the case of TrES-2, TrES-4 and HAT-P-7 have been investigated by Daemgen et al. (2009) and Bergfors et al. (2013) and have been found to be not significant. Under the assumptions above, we derived physical separations, spectral types and masses for the companions to TrES-2, TrES-4 and HAT-P-7 that are in agreement with previous results (see Tables 5 and 6). For the companion to CoRoT-2, the 2MASS magnitudes are $J = 12.866 \pm 0.033$, $H = 12.234 \pm 0.044$ and $K = 12.028 \pm 0.031$. Using the published distance of CoRoT-2 and the models from Kraus & Hillenbrand (2007), we obtain a spectral type of M0 ($\pm$1 SpT), in agreement with the estimate by Schröter et al. (2011).

The candidate companion to CoRoT-3 is also visible in 2MASS images Cutri et al. 2003, and both stars are classified as 2MASS J19281330+0007135 and 2MASS 19281326+0007185, respectively. The near-IR magnitudes of CoRoT-3 are $J = 14.027 \pm 0.036$, $H = 13.448 \pm 0.045$ and $K = 13.295 \pm 0.043$. The separation between the objects given in the 2MASS catalogue is 5.1 ± 0.1 arcsec, in position angle 173°, which are in good agreement with the value of 5.24 ± 0.03 arcsec obtained in this work. Our chance alignment probability for CoRoT-3 is the highest amongst the values derived in this work; however, the proper motions from the Naval Observatory Merged Astrometric Dataset catalogue (Zacharias et al. 2005) for CoRoT-3 are $\mu_\alpha = -10.7 \pm 5.6$ mas yr^{-1} and $\mu_\delta = 21.8$ mas yr^{-1}, which over the 9 yr span between the 2MASS and our observations give a total proper motion of about 0.2 arcsec. Therefore, our results are consistent with the candidate companion being bound to CoRoT-3. Assuming that the object is at the same distance as CoRoT-3, we derive a spectral type of K4–K5 (see Table 4).

7 SUMMARY

To date, several different hypotheses have been formulated in order to explain the observed properties of planetary systems. Compared to our own Solar system, gas giant planets have been found with very short period orbits ($P < 10$ d) posing the problem and at the same time, providing evidence of planetary migration (Lin et al. 1996; Wu & Murray 2003; Ida & Lin 2004; Nagasawa et al. 2008; Marzari & Nelson 2009). The existence of giant planets in highly eccentric orbits and the measurements of their spin–orbit (mis)alignments demonstrate that there must be a number of mechanisms capable of shaping the system orbital configuration. Although evidence for such mechanisms has been provided (Hébrard et al. 2010; Narita et al. 2010; Schlaufman 2010; Triaud et al. 2010; Winn et al. 2010), it is not yet clear which specific mechanisms are more important or act at a particular time to sculpt the configuration of known planetary systems. Recently, Albrecht et al. (2012) suggested that the Kozai mechanism is responsible for the migration of the majority, if not all, hot Jupiters, those misaligned as well as those aligned, and that star–planet tidal interaction plays a central role in shaping exoplanets orbital configurations. Moreover, Narita et al. (2012) suggest that the presence of the two bound companion stars to HAT-P-7 can provide an explanation of the planetary misaligned orbit via sequential Kozai migration (Takeda, Kita & Rasio 2008). Thus, the detection of faint companions to the planet hosts will provide important observational evidence, fundamental for the understanding of the formation and evolution of their planetary systems.

We have investigated the presence of faint stellar companions within 6.5 arcsec of 16 host stars of transiting exoplanets by means of the Lucky imaging technique. We show that this technique has the potential to detect faint stellar companions within the seeing disc (<1 arcsec) of bright primary stars.

We have identified faint candidate stellar companions to six planet hosts. Over the range of brightness of the selected planet host stars in our sample ($3.50 < M_{i'} < 5.47$, i.e. $7.65 < V < 14$), we give 4σ detection limits for putative companions at increasing separations of 0.25, 0.5, 1, 2.5 and 6.5 arcsec from the centre of the primary. For the targets with no detections, we are able to exclude stellar companions of spectral types between M1 and M8 at separations >1 arcsec, depending on the brightness of the primary and the seeing at which the object was observed (see Fig. 4).

We have identified two faint candidate companions to the planet host TrES-1 that have not been previously reported, and our statistical analysis suggests that these stars could be bound to the planet host. Assuming that all the candidate companions are bound to the planet hosting stars, we used the known distances together with models from Kraus & Hillenbrand (2007), and models from Baraffe et al. (1998) to estimate spectral types and masses. In the case of TrES-1, we find the first companion at separation 4.95 ± 0.03 arcsec to be of spectral type M5 ($\pm$1SpT) implying a mass of 0.15 M$_\odot$. The second at separation of 6.19 ± 0.03 arcsec is found to be of spectral type M5 and mass between 0.2 and 0.15 M$_\odot$. In the case of CoRoT-3, we obtain a spectral type of K4–K5 and a stellar mass between 0.75 and 0.7 M$_\odot$ for the candidate companion. For TrES-2, TrES-4, HAT-P-7 and CoRoT-2, we confirm both known candidates as well as bound companions and our estimated spectral types and masses agree with those found by Daemgen et al. (2009), Bergfors et al. (2013), Narita et al. (2010, 2012) and Schröter et al. (2011). Overall, for our targets the epoch of observations either coincide with that of previous works (e.g. Narita et al. 2012; Bergfors et al. 2013), or only allow a short temporal separation with respect to archival and published observations. Given the precision of our astrometry and the relative proper motions of the target stars this does not allow any robust conclusion on the binarity of the detected companions. Therefore, additional high-resolution high-contrast imaging observations are necessary in order to robustly confirm if the companions observed in this and previous works are bound the planet host stars.

Finally, we discuss in Appendix A, the cases of HD 209458, HAT-P-5 and HAT-P-6, for which possible stellar companions were initially visual identified in our images but subsequently classified as non-detections after further analysis was carried out.

ACKNOWLEDGEMENTS

Based on observations made with the NOT, operated on the island of La Palma jointly by Denmark, Finland, Iceland, Norway and Sweden, in the Spanish Observatorio del Roque de los Muchachos of the Instituto de Astrofisica de Canarias. This publication makes use of data products from the 2MASS, which is a joint project of the University of Massachusetts and the Infrared Processing and Analysis Center/California Institute of Technology, funded by the National Aeronautics and Space Administration and the National Science Foundation. FF would like to thank STFC for support through the award of a PDRA as part of the QUB Rolling Grant for Astrophysics. YGMC acknowledges postdoctoral funding support from the Vanderbilt Office of the Provost, through the Vanderbilt Initiative in Data-intensive Astrophysics (VIDA) and through a grant from the Vanderbilt International Office in support of the Vanderbilt-Warwick Exoplanets Collaboration.

REFERENCES

Albrecht S. et al., 2012, ApJ, 757, 18
Alonso R. et al., 2008, A&A, 482, L21
Anderson D. R. et al., 2010, ApJ, 709, 159
Bakos G. Á. et al., 2007, ApJ, 656, 552
Bakos G. Á. et al., 2009, ApJ, 707, 446
Baldwin J. E., Tubbs R. N., Cox G. C., Mackay C. D., Wilson R. W., Andersen M. I., 2001, A&A, 368, L1
Baraffe I., Chabrier G., Allard F., Hauschildt P. H., 1998, A&A, 337, 403
Bergfors C. et al., 2013, MNRAS, 428, 182
Boccaletti A., Chauvin G., Lagrange A.-M., Marchis F., 2003, A&A, 410, 283
Boccaletti A., Riaud P., Baudoz P., Baudrand J., Rouan D., Gratadour D., Lacombe F., Lagrange A.-M., 2004, PASP, 116, 1061
Bochanski J. J., Hawley S. L., Covey K. R., West A. A., Reid I. N., Golimowski D. A., Ivezić Ž., 2010, AJ, 139, 2679
Brandner W. et al., 2000, AJ, 120, 950
Burrows A., Hubeny I., Budaj J., Hubbard W. B., 2007, ApJ, 661, 502
Chatterjee S., Ford E. B., Matsumura S., Rasio F. A., 2008, ApJ, 686, 580
Crida A., Sándor Z., Kley W., 2008, A&A, 483, 325
Crossfield I. J. M., Barman T., Hansen B. M. S., Tanaka I., Kodama T., 2012, ApJ, 760, 140
Cutri R. M. et al., 2003, VizieR Online Data Catalog, 2246, 0
Daemgen S., Hormuth F., Brandner W., Bergfors C., Janson M., Hippler S., Henning T., 2009, A&A, 498, 567
Deleuil M. et al., 2008, A&A, 491, 889
Dhital S., West A. A., Stassun K. G., Bochanski J. J., 2010, AJ, 139, 2566
Diolaiti E., Bendinelli O., Bonaccini D., Close L., Currie D., Parmeggiani G., 2000, A&AS, 147, 335
Dolphin A. E., 2000, PASP, 112, 1383
Eggenberger A., Udry S., Mayor M., 2004, A&A, 417, 353
Fabrycky D., Tremaine S., 2007, ApJ, 669, 1298
Fortney J. J., Marley M. S., Barnes J. W., 2007, ApJ, 659, 1661
Fried D. L., 1978, J. Opt. Soc. Am., 68, 1651
Fruchter A. S., Hook R. N., 2002, PASP, 114, 144
Gillon M. et al., 2010, A&A, 511, A3
Guillot T., 2005, Ann. Rev. Earth. Planet. Sc., 33, 493
Hardy J. W., 1998, Adaptive Optics for Astronomical Telescopes. Oxford Univ. Press, New York
Hébrard G. et al., 2010, A&A, 516, A95
Hinkley S. et al., 2007, ApJ, 654, 633
Høg E. et al., 2000, A&A, 355, L27
Ida S., Lin D. N. C., 2004, ApJ, 604, 388
Jurić M. et al., 2008, ApJ, 673, 864
Kraus A. L., Hillenbrand L. A., 2007, AJ, 134, 2340
Law N. M., Mackay C. D., Baldwin J. E., 2006, A&A, 446, 739
Lee M. H., Peale S. J., 2002, ApJ, 567, 596
Lin D. N. C., Bodenheimer P., Richardson D. C., 1996, Nat, 380, 606
Liu X., Burrows A., Ibgui L., 2008, ApJ, 687, 1191
Mackay C. D., Baldwin J., Law N., Warner P., 2004, in Moorwood A. F. M., Iye M., eds, Proc. SPIE Vol. 5492, High-Resolution Imaging in the Visible from the Ground without AO: New Techniques and Results. SPIE, Bellingham, p. 128
Madhusudhan N. et al., 2011, Nat, 469, 64
Majewski S. R., Skrutskie M. F., Weinberg M. D., Ostheimer J. C., 2003, ApJ, 599, 1082
Marois C., Nadeau D., Doyon R., Racine R., Walker G. A. H., 2003, in Martín E., ed., IAU Symp. 211, Brown Dwarfs. Astron. Soc. Pac., San Francisco, p. 275
Marzari F., Nelson A. F., 2009, ApJ, 705, 1575
McLaughlin D. B., 1924, ApJ, 60, 22
Morton T. D., Johnson J. A., 2011, ApJ, 729, 138
Nagasawa M., Ida S., Bessho T., 2008, ApJ, 678, 498
Narita N. et al., 2010, PASJ, 62, 779
Narita N. et al., 2012, PASJ, 64, L7
Pont F., Hébrard G., Irwin J. M. o., 2009, A&A, 502, 695
Rasio F. A., Ford E. B., 1996, Sci, 274, 954
Rossiter R. A., 1924, ApJ, 60, 15
Schlaufman K. C., 2010, ApJ, 719, 602
Schröter S., Czesla S., Wolter U., Müller H. M., Huber K. F., Schmitt J. H. M. M., 2011, A&A, 532, A3
Skrutskie M. F. et al., 2006, AJ, 131, 1163
Staley T. D., Mackay C. D., 2010, in McLean I. S., Ramsay S. K., Takami H., eds, Proc. SPIE, Vol. 7735, SPIE, Data Reduction Strategies for Lucky Imaging. SPI, Bellingham, 77355Z
Stetson P. B., 1987, PASP, 99, 191
Takeda G., Kita R., Rasio F. A., 2008, ApJ, 683, 1063
Tokovinin A., 2002, PASP, 114, 1156
Triaud A. H. M. J. et al., 2010, A&A, 524, A25
Tubbs R. N., Baldwin J. E., Mackay C. D., Cox G. C., 2002, A&A, 387, L21
Watson C. A., Littlefair S. P., Diamond C., Collier Cameron A., Fitzsimmons A., Simpson E., Moulds V., Pollacco D., 2011, MNRAS, 413, L71
Weidenschilling S. J., Marzari F., 1996, Nat, 384, 619
Winn J. N., 2010, Exoplanet Transits and Occultations. Univ. Arizona Press, Tucson, p. 55
Winn J. N., Johnson J. A., Albrecht S., Howard A. W., Marcy G. W., Crossfield I. J., Holman M. J., 2009a, ApJ, 703, L99
Winn J. N., Johnson J. A., Albrecht S., Howard A. W., Marcy G. W., Crossfield I. J., Holman M. J., 2009b, ApJ, 703, 2091
Winn J. N., Fabrycky D., Albrecht S., Johnson J. A., 2010, ApJ, 718, L145
Winn J. N. et al., 2011, AJ, 141, 63
Wu Y., Murray N., 2003, ApJ, 589, 605
Zacharias N., Monet D. G., Levine S. E., Urban S. E., Gaume R., Wycoff G. L., 2005, VizieR Online Data Catalog, 1297, 0

APPENDIX A: NON DETECTIONS WITH VISUAL IDENTIFICATIONS

(i) HD 209458. For the planet host star HD 209458, slight aberration effects are evident in our images resulting from small-scale mirror irregularities of the NOT, and chromatic dispersion effects (Law et al. 2006). These effects are more pronounced in the images of bright targets like HD 209458 ($V = 7.63$; Høg et al. 2000). The possible detection was present in all four stages of our image analysis at a separation of 1.66 arcsec (within the seeing disc of the primary star) and position angle $241 \pm 1^{\circ}$with $\Delta i' = 7.57$ (SNR ~ 20). Fig. A1 presents the PSF subtraction and the Gaussian convolution steps for HD 209458 showing evidence of the non-axisymmetric PSF, and of the possible detection. Fig. A2 shows our sensitivity as a function of separation from the centre of the primary target. Our possible detection is well above our sensitivity limit at the separation of 1.66 arcsec. However, any identification in our images within the seeing disc of the planet host is investigated further for possible artefacts. VLT+NACO images in the H band for HD 209458 are publicly available from the ESO archive.[4] Our analysis of these NACO near-infrared AO data do not show any evidence of a stellar companion at the position of our possible detection. We would have expected any stellar companion to be brighter in the near-infrared, and thus be readily identifiable in the NACO photometry. This is also in agreement with the non-detection in the Lucky imaging observations by Daemgen et al. (2009) and Bergfors et al. (2013). Therefore, we conclude that the possible detection is most

[4] ESO Archive: http://archive.eso.org/cms.html.

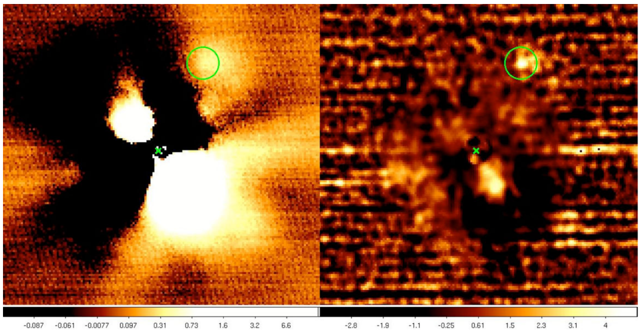

Figure A1. Spurious detection for HD 209458 at a separation of 1.66 arcsec with a $\Delta i' = 7.57$. Left-hand panel: image after PSF subtraction (Step 1 of image analysis). Right-hand panel: image after Gaussian convolution (Step 3). The green cross marks the centre of the primary star, whereas circled in green is the spurious detection most likely due to our image quality.

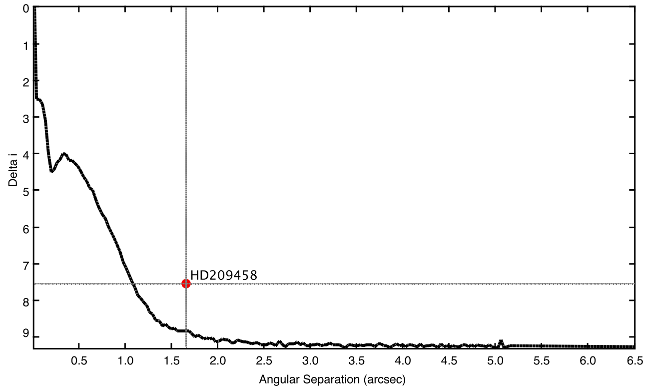

Figure A2. Sensitivity curve as function of distance from the primary plant host star HD 209458 derived for the 5 per cent best-frame selection. The vertical and horizontal grey-solid lines indicate the angular separation (r = 1.66 arcsec), and $\Delta i' = 5.57$ of the possible detection, respectively. Our sensitivity at the angular separation of 1.66 arcsec is $\Delta i' = 8.9$.

likely spurious due to the limited image quality for HD 209458, resulting from the seeing conditions, the number of frames, and the optical characteristics of the NOT.

(ii) HAT-P-5. During our image analysis procedure and visual inspection of the images for the planet host HAT-P-5, we have identified a candidate companion with $\Delta i' = 7.9$ (SNR∼1.9) at a separation of 4.25 arcsec from the centre of the primary star and position angle 268°.5 ± 0°.4. Fig. A3 shows the image from the 5 per cent best LuckyCam frames for HAT-P-5 (left) and the Step 3 (right) of the image analysis where the candidate companion is clearly visible. The measured $\Delta i'$ is 0.14 mag below our 4σ detection cutoff at the separation of 4.25 arcsec, thus it was classified as a non-detection.

(iii) HAT-P-6. In the images of the planet host HAT-P-6, a candidate companion with $\Delta i' \approx 10.7$ (corresponding to a SNR ∼ 0.4) at a separation of 6.4 arcsec is identified by visual inspection. For example, Fig. A4 shows the LuckyCam images for Step 1 (left) and Step 3 (right) of the image analysis where the candidate companion is clearly visible. However, the measured $\Delta i'$ of the putative companion is more than one magnitude below the 4σ detection threshold at that separation from the centre of the primary (see Table 2), thus it is considered a non-detection.

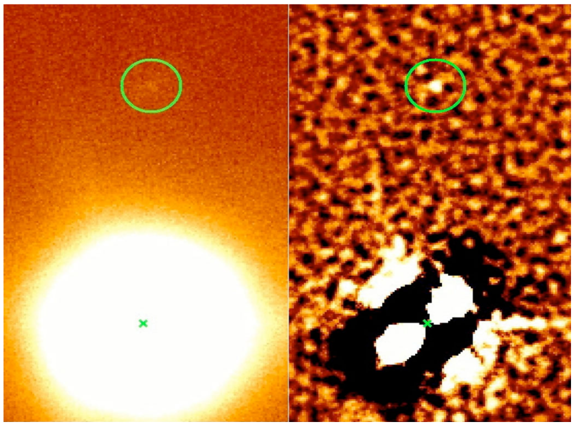

Figure A3. Non-detection for HAT-P-5. Left-hand panel: LuckyCam 5 per cent-frame selection image for HAT-P-5 (Step 1). Right-hand panel: the Gaussian convolution image (Step 3). The green cross marks the location of the centre of the primary star, the tentative companion is circled in green.

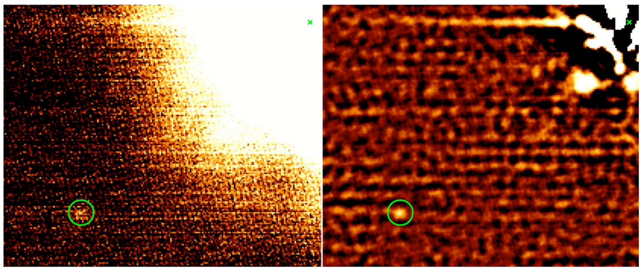

Figure A4. Non-detection for HAT-P-6. Left-hand panel: LuckyCam 5 per cent-frame selection image for HAT-P-6 (Step 1). Right-hand panel: the Gaussian convolution image (Step 3). The green cross marks the location of the centre of the primary star, the tentative companion is circled in green.

In the case of HAT-P-5 and HAT-P-6, our image sensitivity does not allow us to reliably detect the putative companions. However, because our images clearly show the presence of possible companions at large separations from the primary, these might be real and worth further investigation.

This paper has been typeset from a TEX/LATEX file prepared by the author.